Polymer Testing 49 (2016) 137–146

Contents lists available at ScienceDirect

Polymer Testing

journal homepage: www.elsevier.com/locate/polytest

Material behaviour

Comparison of voiding mechanisms in semi-crystalline polyamide 6 during tensile and creep tests

Nathan Selles [a, *], Franck Nguyen [a], Thilo F. Morgeneyer [a], Henry Proudhon [a], Wolfgang Ludwig [b], Lucien Laiarinandrasana [a]

[a] MINES ParisTech, PSL Research University MAT-Centre des Matériaux, CNRS UMR7633, BP 87, 91003 Evry Cedex, France
[b] European Synchrotron Radiation Facility, BP 220, 38043 Grenoble Cedex, France

ARTICLE INFO

Article history:
Received 24 September 2015
Accepted 23 November 2015
Available online 27 November 2015

Keywords:
Semi-crystalline polymers
X-ray tomography
Void anisotropy
Creep

ABSTRACT

Behaviour of a semi-crystalline polymer, polyamide 6, described by loading curves, as well as necking and whitening phenomena, is related to its micro-structural evolution in terms of void morphology and distribution during both tensile and creep tests. Notched bars have been subjected to creep tests interrupted at the onset of the tertiary creep stage and at the onset of final rupture. Inspections of these specimens using Synchrotron Radiation Tomography have been coupled with statistical image analysis treatment to obtain spatial distributions of void length and void volume fraction. Cavitation mechanisms observed and quantified during creep and tensile tests were similar: from penny shaped voids (diameter larger than height) perpendicular to the drawing direction to cylindrical voids (diameter equal to the height) arranged in columns during the neck extension. The void volume fraction distributions along radial and axial directions presented an inverted parabolic profile with a maximum located at the centre of the sample.

1. Introduction

The present paper addresses the question of the durability of polymeric engineering structures such as pressure vessels or pipes submitted to sustained internal pressure for tens of years (50 years). Such structures are subjected to creep loading under a multiaxial stress state. Creep tests at low stress levels require several years and cannot be easily programmed in a laboratory. Moreover, the methodology used to predict lifetimes is nowadays based on extrapolation hypotheses that may be questionable. Indeed, some premature failures of these structures are regularly observed [1]. The macroscopic and viscoelastic behaviours of semi-crystalline polymers subjected to creep loading and slow crack growth are widely studied in the literature [2–4]. However, very few studies about damage mechanisms and cavitation phenomenon within these materials deformed under constant load have been published [5]. In this paper, the methodology suggested to predict lifetimes of such structures is based on the evolution of the microstructure during creep loading. The technique used here to assess damage features at micrometre resolution was Synchrotron Radiation Tomography (SRT). This technique presents numerous advantages. First, regarding sample preparation, SRT is a non-destructive technique and SRT inspections do not require any preparation, unlike SEM inspections of semi-crystalline polymers [6]. Indeed, the latter must be preceded by cutting the samples (observations of microtomed or cryo-fractured surfaces), Au–Pd coating of these surfaces and sometimes by chemical etching. Moreover, voids can be visualized in 3D and directly in space with precise spatial location with the SRT technique whereas, other existing techniques such as IPSLT [7,8] or X-ray scattering [9] provide only an average value over a prescribed volume (no gradient). This ability to explore the whole volume of a sample also gives access to information through the thickness of the inspected samples and to spatial gradients of the parameters of interest. Such observations can now even be made with nanometre resolution, as shown for HDPE [10] and for PA6 [11].

To enhance void growth and to reproduce a well-controlled multiaxial stress state similar to the ones encountered in engineering structures, creep tests were carried out on notched round bars [12]. Macroscopic data such as creep curves or sample deformation were recorded. Whitening and necking on smooth or notched tensile specimens, which have been observed during

* Corresponding author.
E-mail address: nathan.selles@mines-paristech.fr (N. Selles).

http://dx.doi.org/10.1016/j.polymertesting.2015.11.019
0142-9418/

several studies on semi-crystalline polymers, have been attributed to the presence of voids in the deformed polymeric material [12–14]. Previous works on the same PA6 material have related the onset of whitening with the yield stress during steady strain rate load and at the end of the secondary creep during steady loading [15,16]. Under these conditions, the neck extends in the drawing direction accompanied by void growth. In order to study the microstructural evolution, creep tests were stopped at characteristic stages during the creep loading, allowing 3D through thickness SRT-inspections. Qualitative results were first gathered and are discussed below: void shape evolution and their spatial distributions were studied. These observations have been related to quantitative results on the radial and axial evolution of void volume fraction and void characteristic lengths. The void shape was seen to change from prolate (flattened disks oriented perpendicularly to the drawing direction) to obloid (arrangement in columns of cylindrical voids the height of which increased, in the loading direction). These deformation micromechanisms have been already observed and studied during steady strain rate loading [16,17], and a comparison between these data and the present creep related data is made below.

2. Experimental

2.1. Material description

The material under study was a semi-crystalline polymer: a thermoplastic polyamide 6 (PA6) properties of which have been published elsewhere [18,19]. Modulated Differential Scanning Calorimetry (MDSC) was used to determine the main physico-chemical properties that are recalled here: the glass transition temperature $T_g = 53$ °C, the melting point $T_f = 219$ °C and the crystallinity index $\chi = 43\%$. The examination of specimens by Scanning Electron Microscopy (SEM) after chemical etching revealed the spherulitic microstructure of the material, characterised by a spherical shape and a mean diameter of about 5 μm for the spherulites. An attempt was made to inspect pre-existing voids on PA6 fracture surfaces obtained by cryofractography [15]. SEM images of these surfaces were analysed, leading to an initial void volume fraction estimated at about 1% and a void mean diameter around 0.1 μm.

2.2. Sample preparation

The notch root radius was R = 4 mm for the three samples studied (denoted samples A, B and C). The specimens had gauge section diameter of 7.2 mm and a gauge length of 65 mm. The net (minimal) section diameter was 3.5 mm for Samples A and C and 4 mm for Sample B (Table 1). This geometry leads to a moderate stress triaxiality ratio of about 0.54 in the centre of the notched region of the specimens. These samples were dried until a level of humidity of 0% in the material and stored afterward in a dessicator. Then, they were tested at room temperature (20 °C) and at a relative humidity of 50% using an electromechanical tensile rig, monitoring both axial load and cross-head displacement. The experimental procedure consisted of carrying out a tensile creep test up to failure of the specimen in order to plot the general trends of the creep strain history and to determine the time to creep failure of the PA6 material [18]. Similar to smooth specimen results, creep strain curves obtained on notched round bars exhibited three stages: the creep strain rate decreased rapidly with time (stage I, primary creep), then it reached a steady-state and minimal value (stage II, secondary creep), followed by a rapid increase and fracture (stage III, tertiary creep). The tests presented here were stopped around the second inflexion of the creep strain curve (end of the secondary creep) and during the tertiary creep. The purpose was then to study the microstructure evolution of the specimens by following the same approach as the one applied to monotonic tensile tests [17]. In this loading case, it can be recalled that necking and whitening appear for the same material and geometry at the yield (maximum) stress.

Table 1 summarizes characteristic data for the specimens investigated here. The engineering net stress (σ_{net}) is defined as F/S_0 where F is the load and S_0 is the net section of the notched round bar. The deformed notch opening displacement (δ) is defined as the distance between both notch shoulders. This quantity was measured on the deformed samples represented on Fig. 1a. The Creep Measured Displacement (CMD: Δu_c) is the difference between the applied displacement at the end of the test (u) and at the end of the loading stage (u_1):

$$u = u_1 + \Delta u_c$$

It has been mentioned above that the initial net section radius (R_0) was not the same for the three samples. They are shown in Table 1. The net section radii of the deformed samples (R) were also measured. The creep responses of the material together with the pictures of the deformed specimens are displayed in Fig. 1a. The height of the whitened and necked zone (h_w) was measured on these pictures. The values of δ and R are useful for the sake of normalization. This normalization procedure permits comparison of the results from the different samples.

Sample A had the minimum applied stress level ($\sigma_{net} \approx 71$ MPa). For Sample B, the applied stress was increased ($\sigma_{net} \approx 75.4$ MPa) to reduce the test duration and to study the influence of the stress level on the cavitation. Finally, Sample C was obtained after a long period of creep at a low stress level similar to that applied to Sample A ($\sigma_{net} \approx 71.5$ MPa). Since the applied stress was different for each sample in Fig. 1a, the plot does not reflect at what point from the end of the secondary creep the tests were stopped. First, the end of the secondary creep was identified by studying the evolution of the creep strain rate. Then, for each sample, CMD (Δu_c) and time were normalized by their value at the end of the secondary creep: Δu_{II} and t_{II}, respectively. In Fig. 1b, curves obtained after this normalization procedure are superimposed. It can be clearly observed that samples A and B have been deformed up to the beginning of the tertiary creep as soon as the necking accompanied by whitening appeared in the net section. The necked and whitened zone in the vicinity of the net section were, nevertheless, more extended in Sample B than in Sample A. Samples A and C were submitted to a similar net stress but Sample C has been deformed until a more advanced state of creep deformation, when the tertiary creep was well established, prior to the final rupture.

Table 1
Characteristic measures on deformed samples.

	σ_{net} (MPa)	Δu_c (mm)	δ (mm)	R (mm)	R_0 (mm)	h_w (mm)	$h_w/\delta(-)$
Sample A	71	1.93	8.7	1.58	1.75	0.7	0.08
Sample B	75.4	2.06	8.1	1.81	2	1.5	0.19
Sample C	71.5	3.23	9.4	1.31	1.75	2.5	0.27

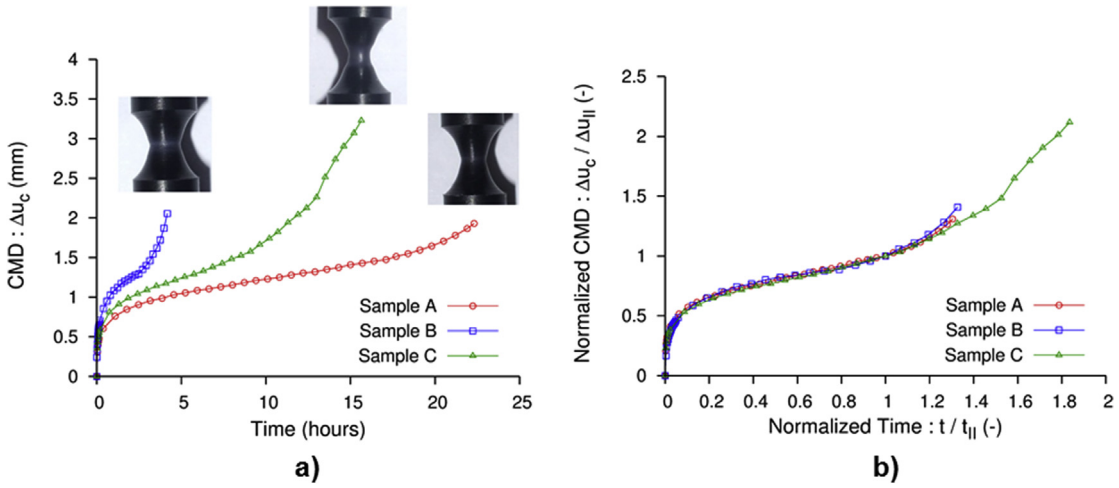

Fig. 1. Sample preparation: (a) Creep Measured Displacement (Δu_c) *vs.* Time and (b) Normalized creep curves.

The microstructure evolution between Sample A and Sample C is supposed to highlight the mode of deformation during the neck extension for a given stress applied.

2.3. Synchrotron radiation tomography (SRT)

2.3.1. Tomography set-up

Inspections of the deformed samples were carried out after at least four months of stress recovery (in an unloaded free state) at the European Synchrotron Radiation Facility (ESRF) in Grenoble (France), using the beamline ID19. The internal microstructure can be observed through the density distribution of the sample and recorded into the reconstructed volumes. Conditions used for these observations were similar to the ones presented in studies of Laiarinandrasana et al. [16,17]: an energy of 17.6 keV and a voxel size of 0.7 μm have been used.

2.3.2. Tomographic volume of interest (TVOI)

The material volume supposed to be observed (diameter of about 3 mm) was larger than the detector's field of view, and the diameter of the maximum reconstructed 3D volume. To avoid the cutting of the samples that can alter their microstructure, a "local tomography" technique has been used [15,16]. Fig. 2b presents the cylindrical volumes of interest (height 358 μm, diameter 716 μm) imaged by SRT and their localisations within the sample. They are depicted by open circles in the horizontal cut view ($r\theta$) and by open rectangles in the longitudinal view (rz). These volumes will be termed the tomographic volume of interest (TVOI); 3 were acquired along the r-direction and 5 or more along z-direction.

2.3.3. Statistical volume of interest (SVOI)

Previous studies of cavitation during steady strain rate loading have revealed gradients for the parameters used to describe the cavitation phenomenon (void volume fraction, cavities height and diameter) through the radial and axial directions within a TVOI [16,17]. A smaller volume of interest, termed statistical volumes of interest (SVOI), was then introduced. To this end, TVOI were virtually cut into 9 × 9 × 9 parallelepipedic SVOI, as illustrated in Fig. 2c. The size of each SVOI was (50 μm × 50 μm × 40 μm). The deformed specimen coordinates system has been used to locate each SVOI.

An image analysis routine was run for each SVOI. It was based on segmentation of grey level images using watershed contour detection. Then, the identification of each void was carried out

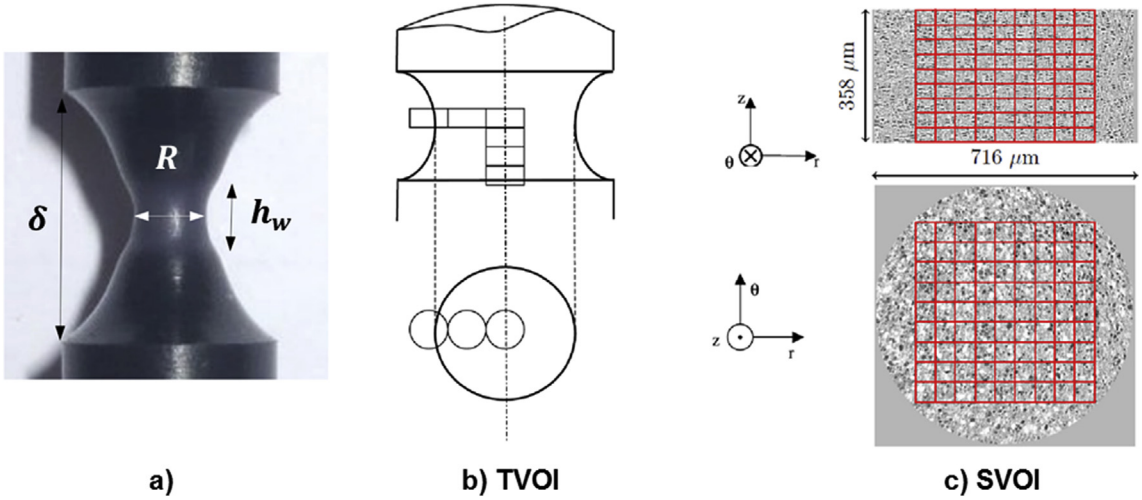

Fig. 2. Sample details for tomographic inspections: (a) Definition of δ, R and h_w (Table 1) on deformed Sample C, (b) Locations of the cylindrical Tomographic Volumes Of Interest (TVOI) defined during local tomography inspections and (c) Description of parallelepipedic Statistical Volumes Of Interest (SVOI) within the TVOI.

thanks to grey level thresholding using local minima [16]. This procedure led to the acquisition of statistical data for each SVOI that was attached to their barycentre in the actual coordinates system. The spatial distribution of parameters of interest, such as void volume fraction (*Vf*) or characteristic void length, was then investigated. *Vf* was defined for each SVOI as the total volume of voids divided by the volume of the whole SVOI. The values of the void volume fraction obtained were subjected to uncertainties due to the image analysis procedure and to the resolution of about 0.7 μm. Indeed, the lower limit of detection was higher than the initial void mean diameter (0.1 μm) and this kind of porosity could not be accounted for in the present determination of *Vf*. The trends of these distributions seem to be more relevant and were studied by normalizing the void volume fraction by its maximum value located in the centre of the net cross section ($z = 0$ and $r = 0$) for the corresponding sample.

3. Results

3.1. Morphology and distribution of voids

3.1.1. In the vicinity of the notch root (surface)

Fig. 3 displays 2D images of Samples A and C in the smallest cross section, near of the notch root. Voids are in black, PA6 matrix is in grey and intervoid walls are in lighter grey or even in white. The distribution of cavities is the same for the two samples and similar phenomena can be observed. Near the notch root, voids are arranged in columns and oriented following the notch root shape. This orientation effect is accompanied by a gradient in void number per volume unit and in void mean diameter when approaching the notch root surface, along the *r*-axis. This gradient leads to a zone with no visible cavitation at the surface of each sample.

3.1.2. In the vicinity of the notch shoulder

From the centre of each sample, in the net cross section, to their shoulder (along *z*-direction), morphology and density of voids show gradients. Fig. 4 illustrates this effect with 2D images through a longitudinal cut of Sample C, but the same evolution has been noticed for the other samples. Getting away from the centre of the specimen, the microstructure (density and morphology of voids) first did not evolve. When the distance to the centre is large enough, the void volume fraction decreases because void height decreases and diameter remains constant (individual void volume decreases). Then, close to the notch shoulder, when the voids are thin enough, the diameters start decreasing. The number of voids per unit volume also decreases to finally reach a microstructure in which cavitation is very punctual.

3.1.3. In the centre

The microstructure in the centre of the net section is represented in Fig. 5 which reproduces, for each sample, a cube of $(140\ \mu m)^3$ volume extracted from the central TVOI. The height of the cube is parallel to the initial load direction.

For Samples A and B, stopped at the onset of the tertiary creep, the void morphology is the same although the two samples were subjected to different net stresses. Voids are in a penny shaped configuration: they have a circular shape in the top view ($r\theta$ cut) that corresponds to the surfaces perpendicular to the loading direction. In the longitudinal view (rz cut), voids are represented by stripes. The intervoids, the matter in lighter grey, have a height larger than those of the voids. Finally, the voids can be seen as flattened disks, diameter of which is larger than the height.

From Sample A to Sample C, that is during the tertiary creep at a similar net stress, voids were observed to extend in height but without shrinking in diameter: this is an anisotropic

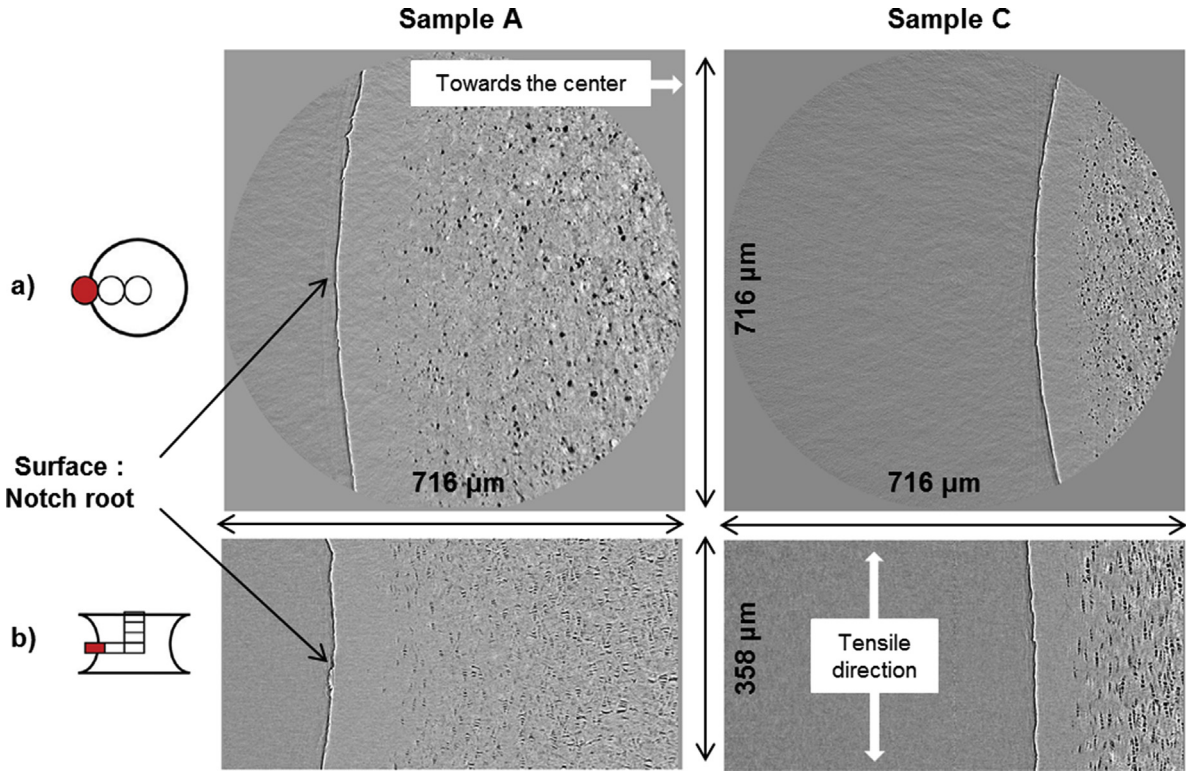

Fig. 3. Distribution of porosity within the net section near of the notch root ($z = 0$ and $r = R$): (a) Top view ($r\theta$) and (b) View through longitudinal cut (rz).

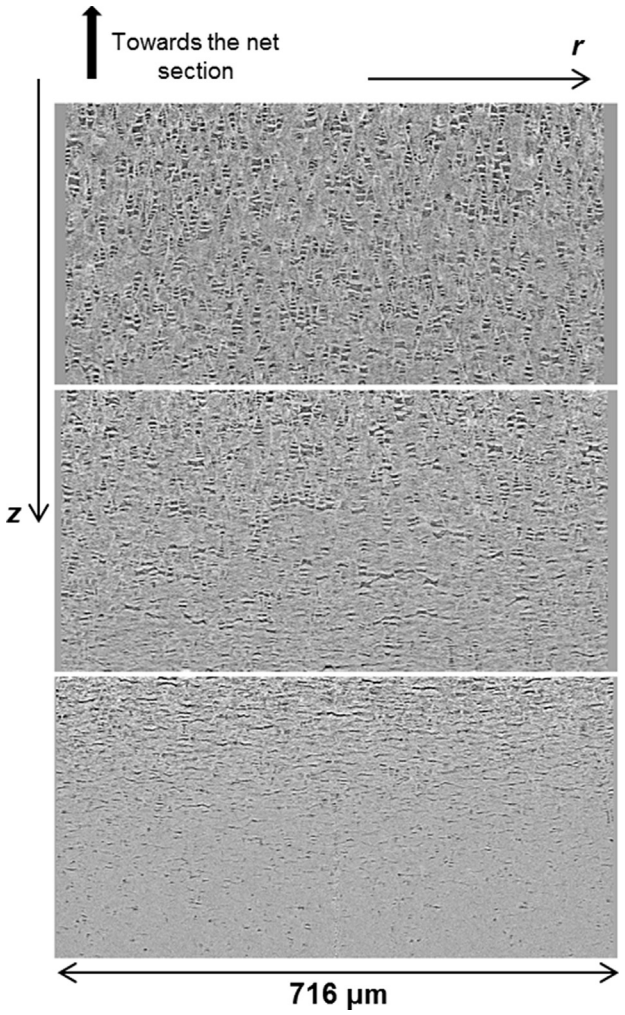

Fig. 4. Distribution of porosity from the centre of the net section to the shoulder of the specimen: view through longitudinal cut (*rz*).

micromechanism of void growth. This shape evolution is consistent with what has been observed using SAXS and IPSLT techniques [20]. The height of intervoids has decreased and the arrangement is in polar fans (columns of voids parallel to the load direction) is systematic. Voids in Sample C can be described as cylinders in the middle of the column, and are conical at the end with height equal to diameter. The bases of these cylinders are circular and perpendicular to the loading direction. This typical arrangement of voids was observed in polypropylene subjected to tensile deformation at a steady strain rate that showed necking [21,22].

3.2. Spatial distributions of void volume fraction (Vf)

3.2.1. Radial distribution

The image analysis procedure presented previously led to a quantitative study of these microstructure evolutions. Normalized void volume fraction has been plotted against current radius r normalized by the net section radius R of the deformed state (Table 1) in Fig. 6a. The sample's axis is represented by the vertical dashed line ($r = 0$) whereas the position of the notch root surface corresponds to the coordinate $r/R = 1$. It can be noted that, for Sample B, the surface was not included in the tomographic scans because its net section had a larger diameter.

The maximum value of Vf is situated in the centre of the net section for all samples. This maximum value increases from Sample A to Sample B but by a small amount (respectively 7 and 9%), whereas the difference between Sample A and Sample C ($Vf_{max} = 13\%$) is more significant. Indeed, the stage of creep reached by Sample C was more advanced than Sample A. Fig. 6a confirms the radial gradient of porosity observed previously that results in a zone where Vf is null from $r/R = 0.95$ to the surface notch root. This parabolic profile has already been encountered for Polyamide 11 microtomed cut samples observed by SEM [6].

3.2.2. Axial distribution

To study the axial distribution of normalized void volume fraction, the axial coordinate z in the deformed state was normalized for each sample by $\delta/2$ (Table 1). Normalized void volume fraction was plotted against $2z/\delta$ in Fig. 6b. The dashed line ($z = 0$) represents the net cross section of the sample. The profile of the curve is parabolic and flattened in the centre for each sample. From the centre to the shoulder, that is when z increases, three zones (Vf is constant, then it decreases until becoming null) can be defined within the sample, as mentioned previously about Fig. 4.

The differences between the three samples are twofold: the value of the maximum void volume fraction located in the centre of the net section and the height of the damaged zone in the load direction. This height increases from Sample A to B and from Sample A to C (0.31, >0.39 and > 0.41 respectively for Samples A, B and C). These values can be compared to the height of the whitened zone, also normalized by δ (Table 1). The whitened zone is systematically less extended than the damaged zone, determined by tomographic inspections. Whitening is a surface phenomenon that

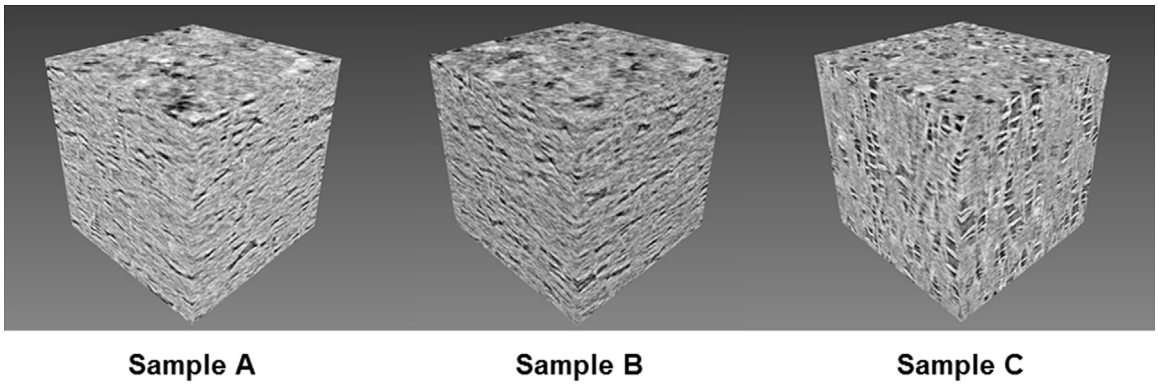

Fig. 5. Morphology of voids in the centre of the samples depending on the stretch before unloading (Sample A *vs.* Sample C) and the stress applied (Sample A *vs.* Sample B). Box size = $(140\ \mu m)^3$.

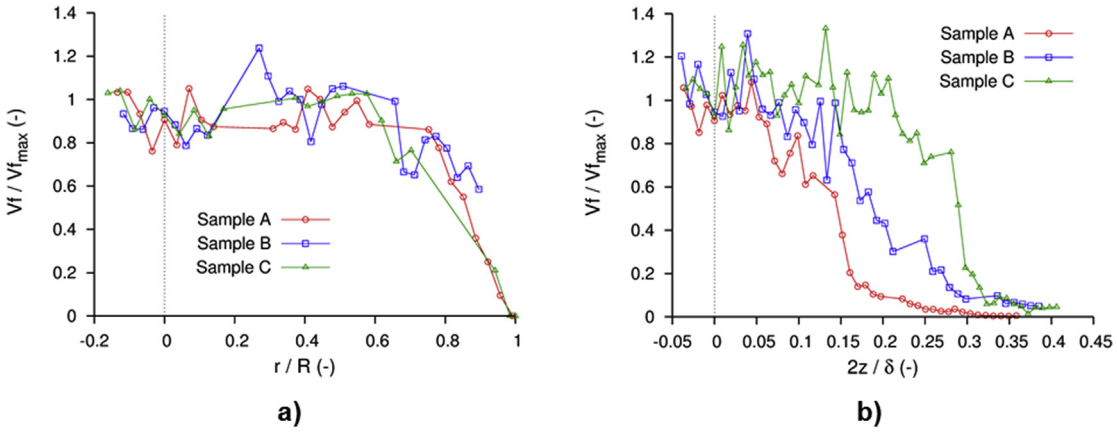

Fig. 6. Trends of radial distribution (a) and axial distribution (b) of void volume fraction *Vf* normalized by Vf_{max} located in the centre of the sample (Vf_{max} = 7%, 9% and 13% respectively for samples A, B and C).

results from the micro-mechanisms and appears after the cavitation that starts inside the specimens.

3.3. Void deformation

Void lengths were measured in the present paper using the Feret lengths [17,23]. Individual cavities were considered as cylinders and this measure consists of diameter and height projections on the macroscopic coordinate axes defined in Fig. 2. These measures have been efficient here because the items did not rotate during the deformation except for the voids located near the notch root surface.

3.3.1. Histograms of void heights and diameters

For each SVOI, an average of 100 cavities have been individually identified, and statistical data corresponding to their position, diameter and height were recorded. The histograms of these characteristic lengths could be plotted for each SVOI. In Fig. 7, data collected for the central SVOI in the net section of each sample have been displayed. To assess the spatial evolution of these characteristic void lengths, a statistical variable that depicts the population studied had to be chosen and then associated with the barycentre of each SVOI. This choice had to take into account the uncertainties on the minimum values, affected by the resolution and the segmentation parameters, and on the maximum ones. Indeed, the Feret measure is not able to distinguish several joined radial voids or to evaluate the effect of void inclination [17]. Three statistical variables were investigated:

- The mean value is the average length calculated on the overall data. Because of the influence of both minimum and maximum lengths on this parameter, it is considered to be subjected to the largest uncertainties;
- The median value is related to a cumulated frequency of 50% by counting increasing length (starting from the minimum length). This value is clearly influenced by the minimum length;
- The mode value is the length corresponding to the maximum frequency. In the following, the analysis is based upon this statistical variable. The mode value seems to be consistent with the qualitative observations that consist in void elongation in the direction of the applied load without any lateral deformation. Moreover, it is the parameter less influenced by the bias introduced by the image analysis routine.

Histograms displayed in Fig. 7 are representative of the trends highlighted previously, and associated mode values and frequencies are given in Table 2. Results for samples A and B were similar, with a maximum frequency of 15% and a mode value around 4 μm for the diameter and, respectively, 35% and 2.1 μm for the height. An evolution is observed from these samples to Sample C. The mode diameter remains unchanged and the maximum frequency slightly decreases, the histogram is flattened and shifted to the higher values. Regarding the mode height, the value increased to 3.5 μm and the histogram of Sample C is less centred on a unique value as for samples A and B.

3.3.2. Radial distribution of void height and diameter

Radial distributions in the net section ($z = 0$) of the mode diameter (left) and the mode height (right) are plotted in Fig. 8 for all samples. The profile of void diameter evolution within the net section is the same for the three samples: an inverted parabola, flattened in the centre where the maximum value (around 4 μm for all samples) is reached. A radial gradient appears at $r/R = 0.8$ and a null value is reached at the notch root surface, in the zone without visible voids. This radial profile is similar to that of the volume fraction. *Vf* decreases because of two phenomena: the decrease of diameter and height of individual cavities and the decrease of number of cavities per unit volume. For the mode height, the radial distributions in the net section of samples A and B are the same. The profile is rectangular: void height is constant from the centre to the end of the voided zone ($r/R = 0.95$) and then, near to the notch surface, drops to zero. This abrupt profile is due to the limited resolution that does not enable taking into account cavities whose height is of the order of a micrometre, characteristic of the cavitation at the notch root surface. Voids in the net section of Sample C have a different height distribution profile. First, void height has increased in the centre of the sample because of the extension of the necked zone along the load direction. Also the profile is "M-shaped" with a maximum value located at $r/R = 0.6$.

3.3.3. Axial distribution of void height and diameter

Fig. 9 displays the axial distributions of the mode diameter (left) and the mode height (right) along the revolution axis of the samples ($r = 0$). Evolutions of void diameter from the centre to the shoulder for all samples are characterized by the same stages for the three samples. First, the diameter is constant, then it decreases and even becomes null for sample A at the coordinate where *Vf* becomes null also. Concerning the axial distribution of void height; results obtained from Sample A and Sample B are very close with a very slight decrease from the centre to the shoulder. The difference

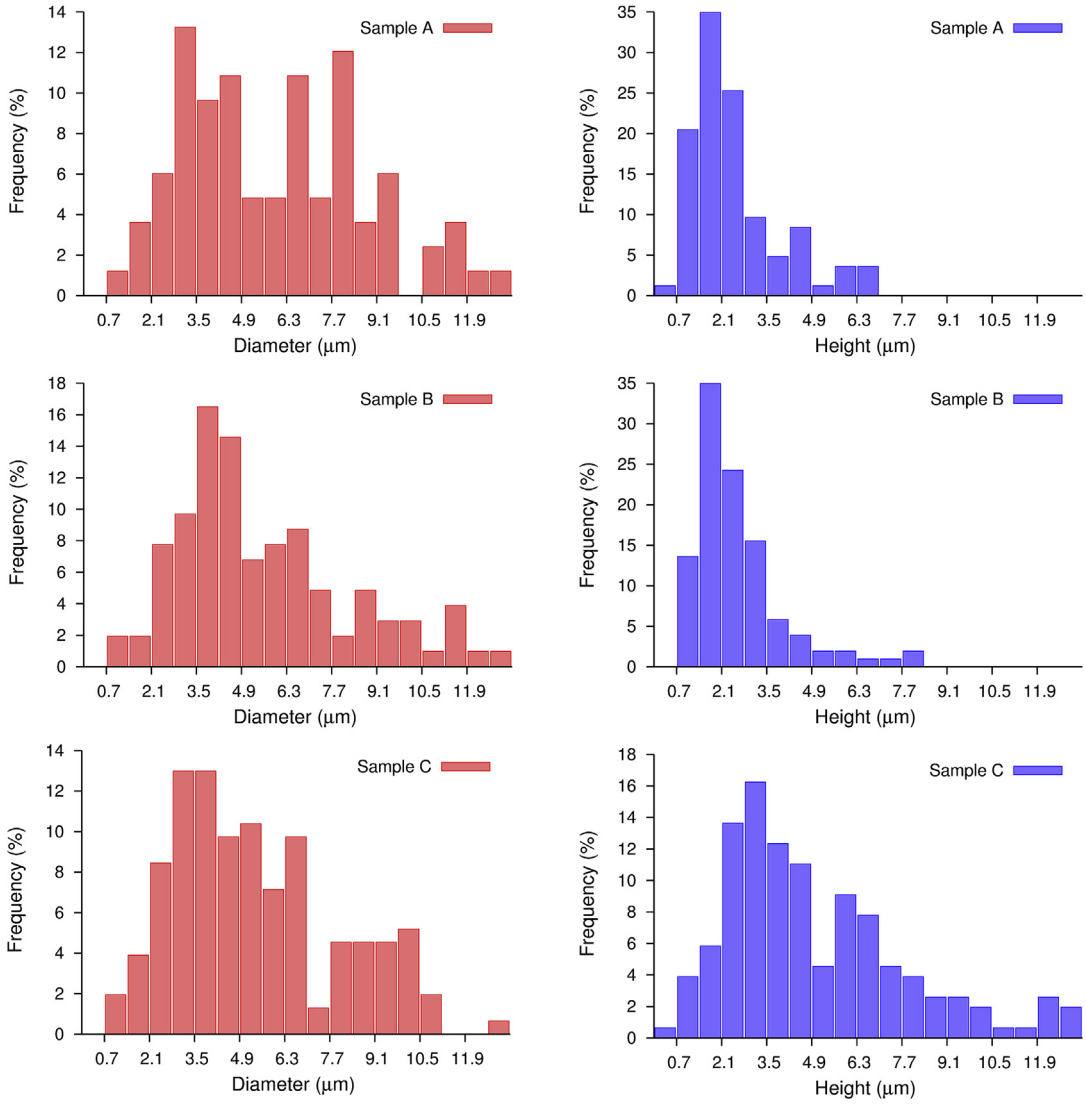

Fig. 7. Histograms of void height and diameter for the central SVOI in the central TVOI for samples A, B and C from top to bottom.

Table 2
Mode values of void diameter and height for the SVOI located in the centre of the net section for samples A, B and C.

	Mode diameter (μm)	Frequency (−)	Mode height (μm)	Frequency (−)
Sample A	3.5	0.135	2.1	0.35
Sample B	4.2	0.165	2.1	0.35
Sample C	3.8	0.13	3.5	0.16

with Sample C comes from the value of this mode height in the centre. Indeed, this axial distribution for Sample C presents the same inverted parabolic profile, flattened in the centre, as the other samples: mode diameter decreases progressively from the centre to the shoulder.

Finally, after the inflexion on the creep curve that occurs during the tertiary creep, voids do not undergo radial deformation (extension or compression) but axial extension, and the diameter seems to be set at a constant value around 4 μm. The increase in void diameter occurs before the onset of the tertiary creep, in an anisotropic way, because radial extension is favoured, leading to "penny shaped" cavities. Moreover, the stress applied during the creep test has no observable effects on the length of voids, unlike the position reached on the creep curve before interrupting the test.

4. Discussion

4.1. Steady load versus steady strain rate: mode of deformation during neck extension

Necking and whitening appear for this PA6 at the yield (maximum) stress on notched round bars subjected to steady strain rate, and at the end of the secondary creep during creep tests on the same notched round bars. This is the first comparison that can be made at the macroscopic scale between these two kinds of loading sequences. In the following we compare the morphology and distribution of voids within samples deformed by a steady load and a steady strain rate and that underwent the same macroscopic changes:

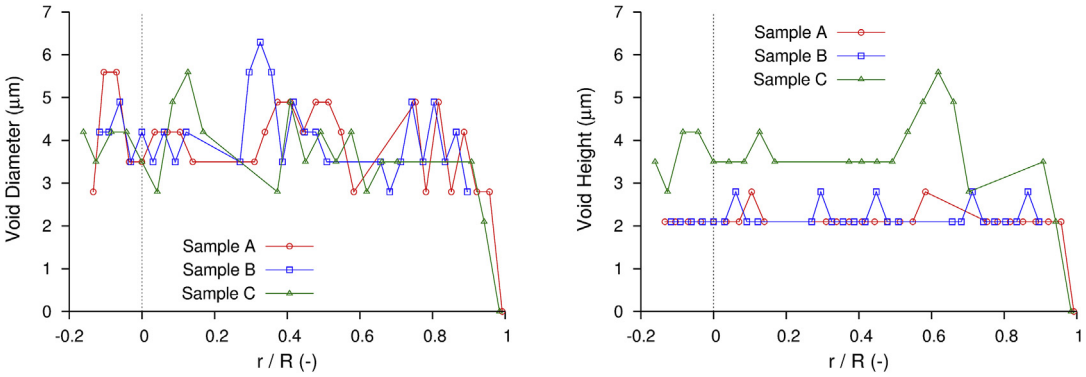

Fig. 8. Radial evolution of void diameter (left) and height (right) for samples A, B and C.

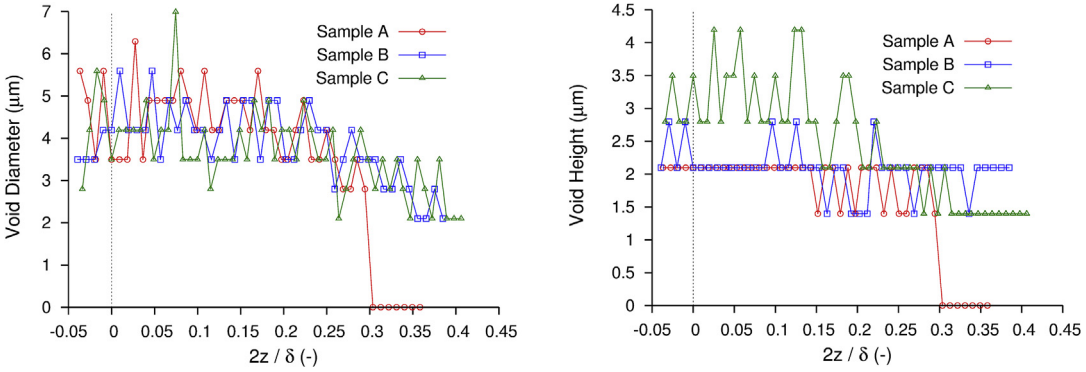

Fig. 9. Axial evolution of void diameter (left) and height (right) for samples A, B and C.

- Onset of necking and whitening at the end of the secondary creep and the yield stress (Sample A respectively for steady load and steady strain rate).
- Extension of the whitened zone until a state prior to the final rupture (Sample C).

This section is dedicated to study the mode of deformation during the neck extension during the tertiary creep for creep tests (comparison between Samples A and C).

The distribution of voids within the net section (orientation effects and zone with no visible cavitation near the notch root) is the same for samples deformed by steady strain rate loading [16] and by steady load. The uniaxial stress state at the notch surface is not favourable for void growth and can explain this zone with no visible cavitation. The evolution of void diameter and height along the axial direction, for these two loading case, leads to similar microstructures in the vicinity of the notch shoulder: voids are spherical and very punctual. In the centre of the samples, the morphology of voids in Sample A, described as flattened disks, the diameter of which is larger than the height, has already been described for a sample deformed by a monotonic tensile test interrupted at the peak stress [16]. Moreover, samples interrupted prior to the final rupture after creep or monotonic tensile tests (Samples C) exhibit the same microstructure: arrangement of voids in columns with cylindrical voids in the middle and conical ones at the end. This evolution can be linked to the extension of the neck. Indeed, in the centre of the sample, the stress state evolves from and moderate triaxial state to a uniaxial state during the tertiary creep, leading to the increase of void height.

The quantitative study confirms the observations obtained from to the tomographic images. The radial and axial distributions of *Vf*, that present flattened parabolic profiles, have been also encountered in monotonic tensile test [16]. These trends have been linked to the stress triaxiality ratio *T*. According to Bridgman relationship [24] and Beremin extension in the axial direction [25], the spatial distributions of *T* present a similar profile, with a maximum located in the centre of the net section and a minimum at the notch root surface. Regarding voids diameter (d) and height (h), results for Sample A are similar to the ones obtained for a monotonic tensile tests interrupted at the peak stress ($d = 5.25$ µm and $h = 1.75$ µm). Voids height for samples deformed until a state prior to the final rupture is also similar for the two kinds of loading (3.5 µm for steady load and 4.5 for steady strain rate). The difference comes from the evolution of the diameter during the neck extension. During monotonic tensile tests, a decrease of the diameter is observed whereas, during creep tests, the diameter remains constant. Finally, the state of creep deformation reached by Sample C is perhaps far from the state prior to the rupture: continuing the test could have led to a larger increase of the height (until 4.5 µm) and to a decrease of the diameter.

Axial and radial distributions of voids characteristic lengths are similar for creep and monotonic tensile tests. Especially for the most deformed samples (sample C), the complex profile of voids height radial distribution can be explained by the radial distribution of the stress triaxiality. Indeed, when the radial coordinate increases, *T* decreases and approaches a uniaxial state that enhanced void stretch along the axial axis. However, this phenomenon is in competition with the decrease in *Vf* and so with the general diminution of voids volume (*Vf* decreases because of a diminution of the voids characteristic lengths and of their number

per unit volume). The competition between the two phenomena leads to this M-like profile for Sample C.

4.2. Modelling and simulation purposes

The visualization of voids in 3D is possible thanks to the SRT technique, whereas other techniques such as SEM or IPSLT give only 2D information [20,21]. To the best of the authors knowledge, it is the first time that such data (spatial distributions of voids characteristic lengths and real void volume fraction) are reported in the literature for creep tests. These data are very useful and very valuable as input for modelling purposes based on the mechanics of porous media. Indeed, the observed anisotropy and void extension along the load direction is not accounted for with constitutive relationships based on the void volume fraction that is representative of spherical void growth only. The simulation of the observed deformation and damage micromechanisms in creep tests could be improved by taking into account the shape and distribution of voids. Such models considered anisotropic void shape as a damage variable [26–28]. Identification of material parameters for these kinds of models, adapted to semicrystalline polymers, could be based on the quantification of the damage parameters shown in the present study to finally take into account the anisotropic void growth.

5. Conclusions

The paper deals with an equivalency of void morphology and distributions for samples deformed under tensile (steady strain rate) and creep (steady load) tests. For steady strain rate, results have been reported elsewhere [16,17]. Creep tests were carried out on PA6 notched round bars for which the multiaxial stress state was well controlled. Ex-situ tests were stopped at characteristic events on the creep curve: at the beginning of the tertiary creep stage (Sample A), and at the onset of the final rupture when the necked region is well extended (Sample C). The stress level has no influence on the cavitation phenomenon. Indeed, the comparison of samples subjected, respectively, to $\sigma_{net} \approx 71$ MPa and 75.4 MPa and deformed until the beginning of the tertiary creep stage lead to similar results. Then, the micromechanisms of deformation during the neck extension for a given applied stress have been assessed with the results obtained for Samples A and C.

The microstructural evolutions were followed using Synchrotron Radiation Tomography, (SRT) allowing 3D through thickness inspections. SRT data processing gives access to the evolution of the void volume fraction (*Vf*) and characteristic void lengths (diameter and height) along the axial and radial directions. The deformed samples exhibited various void morphologies in their centre. Indeed, for Sample A, voids can be represented by flattened disks, perpendicular to the loading direction: void height and diameter are, respectively, about 2.1 μm and 4 μm. This morphology is also encountered at the yield stress during monotonic tensile tests. For Sample C, but also for samples deformed by steady strain rate until the onset of the final rupture, we can observe an increase in void height ($h \approx 3.5$ μm), no shrinking in diameter ($d \approx 3.8$ μm) and a systematic arrangement of cylindrical voids in columns parallel to the loading direction. The distributions of *Vf* observed here are comparable with steady strain rate tensile data [16]. The radial profile is parabolic and flattened in the centre where the maximum value is reached (7 and 13%, respectively, for Samples A and C). The same flattened parabolic profile is encountered for the axial evolution of *Vf*. The evolutions of void lengths are also really close to the ones obtained after monotonic tensile tests [17]. The classical parabolic profile flattened in the centre is observed for the radial and axial distributions of void diameter, and the limited resolution led to quite constant value of voids height along r and z-directions.

Acknowledgement

The authors would like to acknowledge ESRF for beam time in experiment MA1003.

References

[1] C. Devilliers, Dégradation chimique du PE et influence sur le comportement, l'endommagement et la rupture en fluage, Ph.D Thesis, École nationale supérieure des mines de Paris, 2011.
[2] X. Lu, N. Brown, A test for slow crack growth failure in PE under constant load, Pol. Test. 11 (1992) 309–319.
[3] C.J.G. Plummer, A. Goldberg, A. Ghanem, Micromechanisms of slow crack growth in polyethylene under constant tensile loading, Polymer 42 (2001) 9551–9564.
[4] J.L. Gacougnolle, S. Castagnet, M. Werth, Post-mortem analysis of failure in polyvinylidene fluoride pipes tested under constant pressure in the slow crack growth regime, Eng. Fail. Anal. 13 (2006) 96–109.
[5] D. Girard, S. Castagnet, J.L. Gacougnolle, G. Hoschstetter, On the relevance of a notch creep test for the comprehension and prediction of slow crack growth in PVDF, Pol. Test. 26 (2007) 937–948.
[6] G. Boisot, L. Laiarinandrasana, J. Besson, C. Fond, G. Hochstetter, Experimental investigations and modeling of volume change induced by void growth in polyamide 11, Int. J. Solids Struct. 48 (2011) 2642–2654.
[7] R. Schirrer, R. Lenke, J. Boudouaz, Study of mechanical damage in rubber-toughened Poly(Methyl Methacrylate) by single and multiple scattering of light, Polym. Eng. Sci. 37 (1997) 1748–1760.
[8] S. Gehant, R. Schirrer, Multiple light scattering and cavitation in two phase tough polymers, J. Polym. Sci. Part B Polym. Phys. 37 (1999) 113–126.
[9] S. Humbert, O. Lame, J.M. Chenal, C. Rochas, G. Vigier, New insight on initiation of cavitation in semicrystalline polymers: in-situ SAXS measurements, Macromolecules 43 (2010) 7212–7221.
[10] T.F. Morgeneyer, H. Proudhon, P. Cloetens, W. Ludwig, Q. Roirand, L. Laiarinandrasana, E. Maire, Nanovoid morphology and distribution in deformed HDPE studied by magnified synchrotron radiation holotomography, Polymer 55 (2014) 6439–6443.
[11] Y. Cheng, L. Laiarinandrasana, L. Helfen, H. Proudhon, O. Klinkova, T. Baumbach, T.F. Morgeneyer, In Situ Crack Initiation and Propagation in Semicrystalline Polyamide 6 Revealed by 3D Synchrotron Radiation Laminography, Macromol. Chem. Phys. (2015), http://dx.doi.org/10.1002/macp.201500316 (accepted for publication).
[12] S. Castagnet, S. Girault, J. Gacougnolle, P. Dang, Cavitation in strained pvdf : mechanical and x-rays experimental studies, Polymer 41 (2000) 7523–7530.
[13] M. Challier, J. Besson, L. Laiarinandrasana, R. Piques, Damaged and fracture of polyvinylidene fluoride (PVDF) at 20°C : Experiments and modelling, Eng. Fract. Mech. 73 (2006) 79–90.
[14] R. Schirrer, C. Fond, A. Lobbrecht, Volume change and light scattering during mechanical damage in polymethylmethacrylate toughened with core-shell rubber particules, J. Mater. Sci. 31 (1996) 6409–6422.
[15] L. Laiarinandrasana, T. Morgeneyer, H. Proudhon, C. Regrain, Damage of semicrystalline polyamide 6 assessed by 3D X-ray tomography: From microstructural evolution to constitutive modeling, J. Polym. Sci. Part B Polym. Phys. 48 (2010) 1516–1525.
[16] L. Laiarinandrasana, T. Morgeneyer, H. Proudhon, F. N'Guyen, E. Maire, Effect of multiaxial stress state on morphology and spatial distribution of voids in deformed semicrystalline polymer assessed by X-ray tomography, Macromolecules 45 (2012) 4658–4668.
[17] L. Laiarinandrasana, O. Klinkova, T. Morgeneyer, H. Proudhon, F. N'Guyen, W. Ludwig, Three Dimensional Quantification of the Volumetric Strain Anisotropy in Deformed Semi-crystalline Polyamide 6, Int. J. Plast. (2015) (submitted).
[18] C. Regrain, L. Laiarinandrasana, S. Toillon, Experimental and numerical study of creep rupture behavior of PA6, Eng. Fract. Mech. 76 (2009) 2656–2665.
[19] H. Cayzac, K. Saï, L. Laiarinandrasana, Damage based constitutive relationships in semi-crystalline polymer by using multi-mechanisms model, Int. J. Plast. 51 (2013) 47–64.
[20] L. Farge, S. André, P. Pawlak, C. Baravian, S. Irvine, A. Philippe, A study of the deformation induced whitening phenomenon for cavitating and non-cavitating semicrystalline polymers, J. Polym. Sci. Part B Polym. Phys. 51 (2013) 826–841.
[21] A. Pawlak, A. Galeski, Cavitation during tensile deformation of Polypropylene, Macromolecules 41 (2008) 2839–2851.
[22] A. Pawlak, A. Galeski, Cavitation and morphological changes in polypropylene deformed at elevated temperatures, J. Polym. Sci. Part B Polym. Phys. 48 (2010) 1271–1280.
[23] L. Feret, La grosseur des grains de matières pulvérulentes, Premières communications de la nouvelle Association Internationale pour l'essai des matériaux, 1930, pp. 428–436 groupe D.
[24] P. Bridgman, The stress distribution at the neck of a tension specimen, Trans. ASME 32 (1944) 553–574.

[25] F.M. Beremin, Elastoplastic calculation of circumferentially notched specimens using the finite element method, J. Mec. 4 (3) (1980) 307–325.
[26] M. Gologanu, J.B. Leblond, J. Devaux, Approximate models for ductile metals containing spherical oids – case of axisymmetric prolate ellipsoïdal cavities, J. Mech. Phys. Solids 41 (1993) 1723–1754.
[27] M. Gologanu, J.B. Leblond, J. Devaux, Theoretical models for void coalescence in porous ductile solids - II: Coalescence "in columns", Int. J. Solids Struct. 38 (2001) 5595–5604.
[28] T.S. Cao, M. Mazière, K. Danas, J. Besson, A model for ductile damage prediction at low stress triaxialities incorporating void shape change and void rotation, Int. J. Solids Struct. 63 (2015) 240–263.